

Registration of pedobarographic image data in the frequency domain

Francisco P.M. Oliveira^a, Todd C. Pataky^b, João Manuel R.S. Tavares^c

*^aInstituto de Engenharia Mecânica e Gestão Industrial
Faculdade de Engenharia da Universidade do Porto*

Rua Dr. Roberto Frias, s/n

4200-465 PORTO

PORTUGAL

Email: franciscopmoliveira@yahoo.com.br

^bInternational Young Researchers Empowerment Center

Department of Bioengineering, Shinshu University

Tokita, Japan

Email: tpataky@shinshu-u.ac.jp

^cInstituto de Engenharia Mecânica e Gestão Industrial

*Departamento de Engenharia Mecânica, Faculdade de Engenharia da Universidade
do Porto*

Rua Dr. Roberto Frias, s/n

4200-465 PORTO

PORTUGAL

Email: tavares@fe.up.pt

Corresponding author:

Professor João Manuel R. S. Tavares

Departamento de Engenharia Mecânica

Faculdade de Engenharia da Universidade do Porto

Rua Dr. Roberto Frias

4200-465 Porto, PORTUGAL

Phone: +351 225 081 487

Fax: +351 225 081 445

Email: tavares@fe.up.pt, url: www.fr.up.pt/~tavares

Registration of pedobarographic image data in the frequency domain

Abstract:

Image registration has been used to support pixel-level data analysis on pedobarographic image data sets. Some registration methods have focused on robustness and sacrificed speed, but a recent approach based on external contours offered both high computational processing speed and high accuracy. However, since contours can be influenced by local perturbations, we sought more global methods. Thus, we propose two new registration methods based on the Fourier transform, cross-correlation and phase correlation that offer high computational speed. We found out that both proposed methods revealed high accuracy for the similarity measures considered and using control geometric transformations. Additionally, both methods revealed high computational processing speed which, combined with their accuracy and robustness, allows their implementation in near-real-time applications. Furthermore, we found that the current methods were robust to moderate levels of noise, and consequently, do not require noise removal procedure like the contours method do.

Keywords: Biomechanics; Image analysis; Image registration; Fourier transform; FFT, Cross-correlation; Phase correlation; Plantar pressure data; Similarity measures; Robustness

1. Introduction

Image registration is an essential component in several computer vision and image processing tasks. Since each pedobarographic data set can be converted to a rectangular array, image registration computational methods can be used to align the data sets.

When applied to pedobarographic image data, image registration can be an important tool for the clinician because it allows some operations to be made rapidly and automatically. Possible applications include comparison of a pedobarographic image of a particular patient with an image database, and automatic recognition of the foot type of a patient and the assistance in the diagnosis of some common associated pathologies.

Pedobarographic image registration supports pixel-level statistics which, in some situations, can more effectively extract biomechanically-relevant information from plantar pressure images than traditional regional techniques (Pataky et al., 2008a).

Previous studies in pedobarographic image registration (Harrison and Hillard, 2000; Tavares et al., 2000; Bastos and Tavares, 2004; Pinho and Tavares, 2004; Pataky et al., 2008b, c) have been made, but, except for the work described in Harrison and Hillard (2000), they did not focus particularly on implementing computational algorithms in an attractive manner to be used in real automated registration processes, specifically those to be used in real-time analysis of pedobarographic image data. In Oliveira et al. (2009b, 2009c) an automatic contour-based registration method, based on the matching methodology presented in Oliveira and Tavares (2008, 2009a), was implemented to register pedobarographic images. The results showed high accuracy and a dramatically reduced processing time, which allows its use in near-real-time applications.

The computational methods aforementioned present some drawbacks. For instance, the principal axis (PA) transformations (Harrison and Hillard, 2000) is not very accurate, as it was shown by Pataky et al. (2008c); the modal matching (Tavares et al., 2000; Bastos and Tavares, 2004; Pinho and Tavares, 2004) is very sensitive to rotations; the registration method based on the hierarchical implementation of particle swarm optimization made by Pataky et al. (2008c) is very accurate for several similarity measures, but very slow; and the contour-based registration (Oliveira et al.,

2009b,c) is very fast and very accurate for the similarity measure of XOR (Pataky et al., 2008c), however, the MSE accuracy is not so good as in Pataky et al. (2008c). Besides, as that latter method uses just the ordered external contours extracted from the input images, it can suffer from local contours' perturbations and from the presence of feet's shape abnormalities.

In the literature, some robust and fast methods to register images based on the Fourier transform have been presented (Castro and Morandi, 1987; Reddy and Chatterji, 1996; Keller et al., 2005). However, most of those methods assume that the input images are alike; that is, they differ only by transformation and not in their greyscale profiles. The main goal of the current paper was to apply Fourier registration fundamentals to experimental pedobarographic images and to evaluate the accuracy, efficiency, and robustness of the Fourier approach for this purpose.

This paper is organized as follows. In the next section, we describe the methods of cross-correlation (CC), sum of squared differences (SSD) and phase correlation (PC) in the frequency domain; then, in section 3, we present the proposed computational methods and some implementation issues; afterward, experimental results are presented in section 4; finally, in section 5 the results are discussed and some conclusions are pointed out.

2. Theoretical fundamentals

2.1 2D discrete Fourier transform

It is well known that a periodic signal can be represented by a sum of sinusoidal functions. The Fourier transform is a conversion of the signal in the time-domain or space-domain to the frequency-domain. Let f be a greyscale image defined in a 2D $N \times M$ discrete domain, where $f(x, y)$ represents the intensity of the pixel with coordinates (x, y) . Let F be the discrete Fourier transform of f . Thus, F is given by:

$$F(u, v) = \sum_{x=0}^{M-1} \sum_{y=0}^{N-1} f(x, y) e^{-i2\pi \left(\frac{ux}{M} + \frac{vy}{N} \right)}. \quad (1)$$

Therefore, $F(u, v)$ is a complex number, which has the signal amplitude or spectrum $\|F(u, v)\|$ and the phase $\arg(F(u, v))$.

The original image f can be totally reconstructed without loss of information using the inverse Fourier transform:

$$f(x, y) = \frac{1}{MN} \sum_{u=0}^{M-1} \sum_{v=0}^{N-1} F(u, v) e^{i2\pi \left(\frac{ux}{M} + \frac{vy}{N} \right)}. \quad (2)$$

From the two previous equations, it can be seen that the involved computational complexity is $O((NM)^2)$. However, using the fast Fourier transform (FFT) algorithm, the computational complexity of both transforms is $O(NM \log_2(NM))$ (Press et al., 2002).

It is well known that a rotation of an image in the space domain corresponds to a rotation of the spectrum in Fourier domain and a translation in the space domain corresponds to a shift of the phase in Fourier domain (Press et al., 2002; Reddy and Chatterji, 1996). This second property and the convolution theorem are very useful in image registration because they allow the direct estimation of image translation.

In the following sections, we present three methodologies based on the Fourier transform to directly determine the optimal shift between two images. We also present a solution to estimate rotation and scaling transformations.

2.2 Shift determination

We developed three methods to determine the shift that best align two images, all based on the Fourier transform: cross-correlation (CC), sum of squared differences (SSD) and phase correlation (PC), that are explained in the following.

2.2.1 Cross-correlation

Consider two discrete function f and g , in particular two images, and the Pearson's linear correlation coefficient r_{fg} (Press et al., 2002):

$$r_{fg} = \frac{\sum_i (f(i) - \mu_f)(g(i) - \mu_g)}{\sqrt{\sum_i (f(i) - \mu_f)^2} \sqrt{\sum_i (g(i) - \mu_g)^2}}, \quad (3)$$

where μ_f and μ_g are the average intensity of f and g , respectively.

The same coefficient r_{fg} can be given in function of a shift a by;

$$r_{fg}(a) = \frac{\sum_i (f(i) - \mu_f)(g(i-a) - \mu_g)}{\sqrt{\sum_i (f(i) - \mu_f)^2} \sqrt{\sum_i (g(i-a) - \mu_g)^2}}. \quad (4)$$

With the image registration goal, we can assume that the images are best aligned when $r_{fg}(a)$ is maximum; therefore, we search for the value of a that originates the maximum value of r_{fg} . Thus, we can simplify the previous equation by just considering the cross-correlation (CC):

$$CC_{fg}(a) = \sum_i f(i)g(i-a). \quad (5)$$

By the convolution definition, one have:

$$CC_{fg}(a) = \sum_i f(i)\bar{g}(a-i) = \{f * \bar{g}\}(a), \quad (6)$$

where $\bar{g}(i) = g(-i)$ and $*$ represents the convolution. From the convolution theorem, one can obtain:

$$\mathbf{F}\{f * \bar{g}\} = k \cdot \mathbf{F}\{f\} \cdot \mathbf{F}\{\bar{g}\}, \quad (7)$$

where \mathbf{F} represents the Fourier transform and k is a constant that depends on the specific Fourier transform normalization.

Thus, computing the inverse of the Fourier transform (using, for instance, the inverse fast Fourier transform (IFFT)) of the product from Equation (7), the correlation can be obtained for all shifts. Then, the coordinates of the point which has the higher value represent the desired integer optimal shift.

2.2.2 Sum of squared differences

Another approach to translation estimation is based on the sum of squared differences (SSD):

$$\text{SSD}_{fg} = \sum_i (f(i) - g(i))^2. \quad (8)$$

The SSD can be computed in function of a shift a :

$$\begin{aligned} \text{SSD}_{fg}(a) &= \sum_i (f(i) - g(i-a))^2 = \\ &= \sum_i (f^2(i) - 2f(i)g(i-a) + g^2(i-a)) = \\ &= \sum_i f^2(i) - 2\sum_i f(i)g(i-a) + \sum_i g^2(i-a) \end{aligned} \quad (9)$$

Because the assumption behind the SSD is that two images are best aligned when its minimum value is achieved and we are only searching for the optimal shift, SSD equation can be simplified to:

$$\text{PSSD}_{fg}(a) = -2\sum_i f(i)g(i-a) = -2\sum_i f(i)\bar{g}(a-i) = -2\{f * \bar{g}\}(a). \quad (10)$$

Comparing Equation (10) and the cross-correlation of Equation (7), it can be verified that the optimal shift obtained by both methods are the same.

The SSD can be evaluated in a region of interest (ROI), considering the weight function w and rewriting the SSD equation as:

$$\text{SSD}_{fg,w} = \sum_i (f(i) - g(i))^2 w(i). \quad (11)$$

By an analogous process to the one described above, the $\text{SSD}_{fg,w}$ equation can be expanded and the weight SSD can be efficiently computed in Fourier domain, (Orchard, 2007).

2.2.3 Phase correlation

Let us consider two images f and g and their Fourier transforms F and G , respectively, and suppose that $g(x, y) = f(x - x_0, y - y_0)$; thus, according to the shift property (Castro and Morandi, 1987), we can get:

$$G(u, v) = F(u, v)e^{-2\pi i(ux_0 + vy_0)}. \quad (12)$$

Then, by computing the cross-power, we have:

$$\frac{F(u, v)G^*(u, v)}{|F(u, v)G^*(u, v)|} = e^{-2\pi i(ux_0 + vy_0)}, \quad (13)$$

where G^* represents the complex conjugate of G .

By computing the inverse of the Fourier transform of the cross-power, a Dirac δ -distribution centered on (x_0, y_0) is obtained (Castro and Morandi, 1987). Therefore, the coordinates of the Dirac pulse indicate the optimal integer shift. However, when the images differ significantly each other, the phase correlation matrix obtained is not defined by just one pulse but rather by several. Usually several other peaks appear around the highest peak and occasionally the neighbourhood of the highest peak is weaker than the neighbourhood of the others peaks. Thus, we assume that we should choose the highest peak that belongs to the strongest neighbourhood. Consequently, before the search for the highest peak, the phase correlation matrix/image is smoothed using a 3×3 Gaussian kernel with $\sigma = 1.5$.

2.2.4 Subpixel registration

In the literature, there are some methods to extend the accuracy of registration algorithms based on the Fourier transform to subpixel level (Averbuch and Keller, 2002; Hoge, 2003). We interpolate the neighbourhood of the strongest peak using a quadratic function, and then we determine the continuous coordinates associated with the maximum CC or PC value or the minimum SSD value. Additionally, we considered a 3×3 neighbourhood centred on the highest peak and use least squares to compute the coefficients of the quadratic function.

2.3 Rotation and scaling

Any point of the plane with rectangular coordinates (x, y) can be represented in *log*-polar coordinates $(\log_b r, \theta)$, in which $b > 1$ is the base of the logarithm. For simplicity, in the following we omit the base. For any point (x_c, y_c) chosen to be the transformation centre, we have:

$$\log r = \log \sqrt{(x - x_c)^2 + (y - y_c)^2} \quad \text{and} \quad \tan \theta = \frac{y - y_c}{x - x_c}. \quad (14)$$

Let us suppose that we have two similar images f and g , where g is a copy of f rotated by an angle β and scaled by a factor of s ($s > 0$). For simplicity, let us consider that

the rotation and scaling were applied around the origin point. Thus, a point (x, y) in f has in g the coordinates $(s x \cos \beta - s y \sin \beta, s x \sin \beta + s y \cos \beta)$. If the point (x, y) in f has \log -polar coordinates $(\log r, \theta)$, then the same point in g has \log -polar coordinates $(\log(sr), \theta + \beta) = (\log s + \log r, \theta + \beta)$. Thus, a scaling and rotation in a rectangular coordinate system corresponds to a shift in a \log -polar coordinate system. The rotation and scaling properties of the Fourier transform state that a rotation in the space domain corresponds to the same rotation of the spectrum, and a scaling by a factor of $s > 0$ in the space domain corresponds to a scaling by factor $1/s$ in the frequency domain (Press et al., 2002; Reddy and Chatterji, 1996). By the shift property of the Fourier transform, we also know that if two images just differ by a shift, then their spectrum magnitudes are equal.

Through the three properties described above, we know that if two images just differ by a shift, a rotation and a scaling, then their spectrums differ only by a rotation and a scaling. After converting the spectrum to \log -polar coordinates, the rotation and the scaling will be represented by a shift (Wolberg and Zokai, 2000; Keller et al., 2005). Thus, by using the CC, SSD or PC methods previously described, the optimal shift in the \log -polar coordinate system can be determined and consequently, the optimal rotation and scaling in the space domain are obtained.

Because digital images are defined in a discrete grid, to increase accuracy both the base of the logarithm and the angle step should be as small as possible. However, one should remember that increased accuracy will sacrifice computational speed.

3. Methodology

3.1 Algorithm

The current algorithm can be described in eight steps: I) Convert both input images to the frequency domain using FFT; II) Convert both spectrums to \log -polar coordinates; III) Convert both \log -polar spectrum images to the frequency domain using FFT; IV) Determine the optimal shift of the \log -polar spectrums using CC, SSD or PC method (the shift along $\log r$ axis allows to determine the scaling and the shift along θ axis

allows to determine the rotation angle); V) Apply the scaling and rotation to the source image; VI) Convert the transformed image to the Fourier domain using FFT; VII) Use the CC, SSD or PC method to determine the optimal shift between the template image and the rotated/scaled source image; VIII) Apply the computed rotation, scaling and shift to the original source image.

In Figure 1 the current cross-correlation algorithm is depicted. In cases where scaling is not necessary, for instance, intra-subject pedobarographic images, in steps II and IV above a simple polar coordinate system is used and the scale factor is set to one.

3.2 Implementation issues

To compute the FFT and the IFFT, we use the algorithms described in (Press et al., 2002). To convert the images to *log*-polar (or polar) coordinates and apply the geometric transformation to the source image, we use bilinear interpolation.

In steps I and III of our algorithm, we applied the FFT algorithm to real data sets with the same dimension. Thus, we exploit the symmetry of the Fourier transform to handle the two real functions (the images) at once. Let us consider two real and discrete functions f and g and their Fourier transforms F and G . Since each $f(n)$ is real, the components of the discrete Fourier transform satisfy $F(N-n) = F^*(n)$, where $*$ denotes complex conjugation (Press et al., 2002). By the same reasoning, the discrete Fourier transform of a purely imaginary set of g has the opposite symmetry $G(N-n) = -G^*(n)$. Thus, if we register both real functions in one complex array, where f is the real part and g is the imaginary part; both Fourier transforms can be computed at the same time and then separated afterward.

Before converting both input images to the frequency domain, it is necessary to pre-pad images with zeros in the following situations (for a detailed explanation see, for instance, Keller et al. (2005)):

- The images do not have the same dimensions;
- The image dimensions are not equal in both axes;
- To avoid wrap-around effects in the frequency domain;
- The image dimensions are not a power of 2 (Press et al., 2002).

The transformation from rectangular coordinates to *log*-polar (or polar) coordinates does not distribute the images' pixels uniformly. In fact, using a rectangular to *log*-polar (or polar) transformation, the pixels near the center have more influence in the *log*-polar image than pixels far from the center, Figure 2. Thus, in the spectrum image the lowest frequencies (near the center) have more influence than the highest frequencies (far from center). Therefore, when the FFT of *log*-polar (or polar) images is computed, a reduced part of the original spectrum image (low frequencies) will have a strong impact on the final results, decreasing the likelihood of achieving good estimators for rotation and scaling. To distribute more uniformly the power spectrum, we multiply the power of each row in *log*-polar (or polar) axis by the distance to the center and the width of the corresponding ring, Figure 2.

3.3 Computational complexity

As was previously described, zero padding is necessary in some situations. Thus, let us consider that the padded images have dimension $N \times N$. To compute the Fourier transform using the FFT algorithm the computational complexity is:

$$O(N^2 \log_2 N^2) = O(2N^2 \log_2 N) \approx O(N^2 \log_2 N). \quad (15)$$

For those images dimensions, two FFT and one IFFT are needed.

To convert the spectrums images to *log*-polar coordinates the complexity depends on the base of the logarithm and the number of angular steps. For instance, regarding an accuracy of 1° in the angle, we need 180 steps as the spectrum image is symmetric, and thus we just use half spectrum image.

The base of the logarithm in the *log*-polar coordinate system defines the minimum value possible for the scale. For instance, if we know that the scaling is greater than 1.05, we do not need to use a value less than 1.05 for the logarithm base. The smaller the logarithm base, the greater the accuracy of the computed scaling value. However, as is shown in subsequent results, we do not need to use extremely small values for the base of the logarithm, because the algorithm used for subpixel accuracy works quite well. Additionally, we used two different grids for the *log*-polar images: $N \times 2^7$ and $N \times 2^8$, that is, we used N steps in the $\log r$ axis and 128 or 256 steps in the θ axis. Using polar coordinates, we just used $N/2$ steps in the r axis.

To convert the complete spectrum image to *log*-polar coordinates, the computational complexity is $O(A \times N)$, where A is the number of different angle values used. The computational complexity to convert the *log*-polar images to the frequency domain is $O(AN \log_2(AN))$.

The computational complexities for the bilinear interpolations are $O(N^2)$ and $O(AN)$. In conclusion, the computational complexity depends on the images to register and the desired level of accuracy for the angle and scale. Thus, the total computational complexity is:

$$O(\max\{N^2 \log_2 N^2; AN \log_2(AN)\}). \quad (16)$$

3.4 Data

Data from a previous study (Pataky et al., 2008c) were here re-analyzed to afford direct comparison between the new and previous methods. The dataset consisted of 30 pairs of peak pressure images, three random image pairs from ten random subjects. The data were originally collected at 500 Hz using a 0.5 m Footscan system (RSscan, Olen, Belgium). Each pedobarographic image was defined in a rectangular grid of 45×63 pixels.

3.5 Registration accuracy assessment using control images

We first assessed registration accuracy by applying known transformations to the set of 30 template images and then comparing these known parameters to those obtained using the above methods. We also assessed robustness to noise by repeating the above experiments after adding controlled Gaussian noise to the input images.

Some current pedobarographic equipment, like the ones based on light refraction techniques (Tavares et al., 2000), can introduce noise in the data acquired with a Gaussian noise distribution. Thus, we decided to test the robustness of our methods to that kind of noise. Therefore, first, we applied a known geometric transformation to a set of 30 images, and then we added Gaussian noise to both image sets, the original images and the transformed images. Finally, both cross-correlation and phase

correlation algorithms were tested on those images. Because we wanted to test the noise robustness of the algorithms, we used the noisy images without any image filtering operation. The noise amplitude used had a Gaussian distribution with zero mean (0 N/cm^2) and standard deviation ranging from 0 to 2.0 N/cm^2 . We note that pedobarographic data intensities are subject-dependent, and consequently, the signal to noise ratio (SNR) is subject-dependent as well.

3.6 Registration quality assessment using experimental images

Registration was repeated on the experimental images pairs (Section 3.4), and speed and accuracy were compared with the global Min(MSE) and Min(XOR) algorithms described in Pataky et al. (2008c) and Geometric and Hybrid algorithms described in Oliveira et al. (2009b). The sensitivity of XOR and MSE was assessed qualitatively for two different angular steps: $180^\circ / 2^7 \approx 1.4^\circ$ and $180^\circ / 2^8 \approx 0.7^\circ$.

For intra-subject registration scaling was not employed, following previous studies (Pataky et al., 2008c; Oliveira et al., 2009b), because plantar foot geometry may be considered relatively constant trial-to-trial for a given subject. In these experiments, we used the polar transformation.

3.7 Inter-subjects registration quality assessment

To test the accuracy on inter-subjects registration of both algorithms, first we chose 10 images, one of each one of the 10 subjects (Section 3.4) and then we register each image with all the other 9 images. In the total, there are 45 different combinations. In those experiments, we consider the scaling effects, and consequently, we used the *log*-polar transformation instead of polar transformation.

3.8 Implementation

The algorithms were implemented in C++, using Microsoft Visual Studio 8 and were tested on a notebook PC with an AMD Turion64 2.0 GHz microprocessor, 1.0 GB of RAM and running Microsoft Windows XP.

4. Results

In this section CC and the PC results are presented. SSD results are not presented because they are equivalent to the CC results, as previously explained (Section 2.2.2).

4.1 Accuracy

4.1.1 Control images

The two Fourier methods were highly accurate for controlled transformations, Table 1. Figure 3 shows two examples.

Both methods were also very accurate in the presence of Gaussian noise with amplitude zero mean (0 N/cm^2) and standard deviation ranging from 0 to 1.5 N/cm^2 , Table 2. For the 30 images pairs used, the SNR of pedobarographic image data varied between 4.1 and 10.4 for Gaussian noise with standard deviation $\sigma = 0.5 \text{ N/cm}^2$ and between 1.4 and 3.5 for Gaussian noise with standard deviation $\sigma = 1.5 \text{ N/cm}^2$.

The average rotation, scale and translation were practically identical to the values obtained without noise addition. However, we found that the noise standard deviation increases caused increased variation in transformation parameter estimation. The cross-correlation algorithm performed slightly better than the phase correlation algorithm. Parameter estimation performance decreased for noise standard deviation equal or greater than 2.0 N/cm^2 .

4.1.2 Intra-subject registration

The current methods performed well for intra-subject registration, Table 3.

4.1.3 Inter-subject registration

The CC and PC methods produced qualitatively good alignment for all inter-subject image pairs (e.g. Figure 5) and also produced identical similarity values (Table 4).

4.2 Speed

Average registration durations per image pair are presented in Tables 1 and 3. These values include all computational tasks, from disk data reading to final image building and similarity measure computing.

5. Discussion and conclusions

The results demonstrate that both cross-correlation and phase correlation registration methods were very rapid and robust to the natural variations found in a random sample of non-pathologic pedobarographic images. Both methods were also very robust and accurate to controlled transformations (Table 1); maximum differences between the applied and estimated values were approximately 0.1° for rotation, 1% for scale and 0.03 pixels for translation. We note that small errors were expected because geometric image transformations produce subtle nonlinear distortions due to interpolation imperfections and pixel-based sampling (e.g. Parker et al., 1983). These results allow us to conclude that both current Fourier based methods are more accurate than the one presented in Oliveira et al. (2009b), which indicates considerably greater differences between applied and estimated transformation parameters.

Tables 1 and 3 reveal that different combinations of angular steps and logarithm bases yield identical results. This fact allows us to conclude that the current neighbourhood polynomial interpolation was adequate. We also conclude that the current Fourier methods are robust to the presence of pixel Gaussian noise (with amplitude of zero mean and standard deviation ranging from 0 to 1.5 N/cm^2) in the input images (Table 2).

Both methods, mainly the CC, produced MSE values identical to the ones obtained in Pataky et al. (2008c), although the cited study had employed powerful global optimization methods, and better than the ones presented in Oliveira et al. (2009b). Regarding the XOR as a similarity measure, none of the presented methods produced better average results than the ones presented in Oliveira et al. (2009b); however, the standard-deviations were considerably lower. This fact allows us to conclude that CC and PC methods are probably more robust than the geometric and hybrid registration methods presented in Oliveira et al. (2009b) that can be affected by local perturbations of the feet shape. In Oliveira et al. (2009c) better XOR results are obtained using a new contours' matching method based on local features, but that work did not focus the main attention in the registration of pedobarographic images, and so no more details are available for a deeper comparison.

Based on visual evaluation, one can conclude that the current methods consistently performed good alignments for inter-subject registration, even when foot shapes were considerably different.

The main advantage of both new methods, when in comparison to some algorithms previously implemented for pedobarographic images (Harrison and Hillard, 2000; Tavares et al., 2000; Bastos and Tavares, 2004; Pinho and Tavares, 2004; Pataky et al., 2008b, 2008c; Oliveira et al., 2009b, 2009c) is the fact that it simultaneously combines high accuracy, robustness and speed. The confirmed robustness and speed of these methods are important for the clinic, where automation and speed are essential. This will make possible the automatic recognition of the foot type of a patient and the assistance in the diagnosis of some common associated pathologies. Additionally, it will allow the automatic identification of important foot regions, based on the regions previously identified in model images.

In our computational implementations, we have considered the standard cross-correlation computation because test images used did not have significant noise and, as shown in Table 2, the registration algorithm is quite robust to noise, even without a preprocessing step of noise removal. Otherwise, we could make an image filtering before registration. Another possible solution could be the use of an alternative cross-correlation presented in Fitch et al. (2005), but the computational costs will have a small increase.

Acknowledgements

The first author would like to thank his PhD grant of the Portuguese Fundação Calouste Gulbenkian.

References

Averbuch, A., Keller, Y., 2002. FFT based image registration. Proceedings of IEEE International Conference on Acoustics, Speech, and Signal Processing, 2002 (ICASSP '02), Orlando, Florida, 4(IV):3608-3611.

Bastos, L. F., Tavares J. M. R. S., 2004. Improvement of modal matching image objects in dynamic pedobarography using optimization techniques. Lecture Notes in Computer Science 3179, Articulated Motion and Deformable Objects. Springer, Berlin: 39-50.

Castro, E., Morandi, C., 1987. Registration of translated and rotated images using finite Fourier transforms. IEEE Transactions on Pattern Analysis and Machine Intelligence 9(5):700-703.

Fitch, A., Kadyrov, A., Christmas, W., Kittler, J., 2005. Fast robust correlation. IEEE Transactions on Image Processing 14(8):1063-1073.

Harrison, A. J., Hillard, P. J., 2000. A moment-based technique for the automatic spatial alignment of plantar pressure data. Proceedings of the Institute of Mechanical Engineers, Part H: Journal of Engineering in Medicine 214(3):257-264.

Hoge, W., 2003. A subspace identification extension to the phase correlation method. IEEE Transactions on Medical Imaging 22(2):277-280.

Keller, Y., Averbuch, A., Isreali, M., 2005. Pseudopolar-based estimation of large translations, rotations, and scalings in images. IEEE Transactions on Image Processing 14(1):12-22.

Oliveira, F., Tavares, J.M.R.S., 2008. Algorithm of dynamic programming for optimization of the global matching between two contours defined by ordered points. *CMES: Computer Modeling in Engineering & Sciences* 31(1):1-11.

Oliveira, F., Tavares, J.M.R.S., 2009a. Matching contours in images through the use of curvature, distance to centroid and global optimization with order-preserving constraint. *CMES: Computer Modeling in Engineering & Sciences* 43(1):91-110.

Oliveira, F., Tavares, J. M. R. S., Pataky, T., 2009b. Rapid pedobarographic image registration based on contour curvature and optimization. *Journal of Biomechanics* 42(15):2620-2623.

Oliveira, F., Tavares, J. M. R. S., Pataky, T., 2009c. A versatile matching algorithm based on dynamic programming with circular order preserving. *VIPimage 2009 – II ECCOMAS Thematic Conference on Computational Vision and Medical Image Processing, Porto, Portugal, 14-16 October, 2009, Taylor and Francis, 269-274.*

Orchard, J., 2007. Efficient least squares multimodal registration with a globally exhaustive alignment search. *IEEE Transactions on Image Processing* 16(10):2526-2534.

Parker, J., Kenyon, R., Troxel, D., 1983. Comparison of interpolating methods for image resampling. *IEEE Transactions on Medical Imaging* 2(1):31-39.

Pataky, T. C., Caravaggi, P., Savage, R., Parker, D., Goulermas, J. Y., Sellers, W. I., Crompton, R. H., 2008a. New insights into the plantar pressure correlates of walking speed using pedobarographic statistical parametric mapping. *Journal of Biomechanics* 41(9):1987-1994.

Pataky, T. C., Goulermas, J. Y., 2008b. Pedobarographic statistical parametric mapping: a pixel-level approach to foot pressure image analysis. *Journal of Biomechanics* 41(10):2136-2143.

Pataky, T. C., Goulermas, J., Crompton, R., 2008c. A comparison of seven methods of within-subjects rigid-body pedobarographic image registration. *Journal of Biomechanics* 41(14):3085-3089.

Pinho, R., Tavares J. M. R. S., 2004. Dynamic pedobarography transitional objects by Lagrange's equation with FEM, modal matching and optimization techniques. Lecture Notes in Computer Science 3212, Image Analysis and Recognition. Springer, Berlin, 92-99.

Press, W., Teukolsky, S., Vetterling, W., Flannery, B., 2002. Numerical Recipes in C: the art of scientific computing, 2nd edition. Cambridge University Press, USA.

Reddy, B., Chatterji, B., 1996. An FFT-based technique for translation, rotation, and scale-invariant image registration. IEEE Transactions on Image Processing 5(8):1266-1271.

Tavares, J. M. R. S., Barbosa, J., Padilha, A. J., 2000. Matching image objects in dynamic pedobarography. In Proceedings of the 11th Portuguese Conference on Pattern Recognition. Porto, Portugal.

Wolberg, G., Zokai, S., 2000. Robust image registration using log-polar transform. Proceedings of International Conference on Image Processing, Vancouver, Canada, 1:493-496.

FIGURE CAPTIONS:

Figure 1: Cross-correlation algorithm and data pipeline.

Figure 2: Transformation from rectangular coordinates to *log*-polar coordinates.

Figure 3: Two examples of registration using known transformations. By row, from the left to the right: original image; transformed image; overlapped images before registration and overlapped images after registration.

Figure 4: Two examples of registration using control transformation and noise addition ($\sigma = 0.5 \text{ N/cm}^2$ on first row and $\sigma = 1.5 \text{ N/cm}^2$ on second row). By row, from the left to the right: noisy original image; noisy transformed image; overlapped images before registration and overlapped images after registration. (To facilitate the visualization, the original and transformed noisy images were converted to greyscale images; the overlapped images were binarized and the background was turned to white.)

Figure 5: Two examples of inter-subject registration. By row, from the left to the right: template image; source image; overlapped images before registration and overlapped images after registration. (To facilitate the visualization, the original and transformed images were converted to greyscale images; the overlapped images were binarized and the background was turned to white.)

TABLE CAPTIONS

Table 1: Comparison between the control values applied to 30 pedobarographic template images and the corresponding values obtained using the cross-correlation (CC) and phase correlation (PC) methods. (SD – Standard deviation, Tx – Translation along x axis, Ty – Translation along y axis)

Table 2: Comparison between the control values applied to 30 pedobarographic template images and the corresponding values obtained using the cross-correlation (CC) and phase correlation (PC) methods in the presence of Gaussian noise ($\bar{x} = 0$; $\sigma = 0.5 \text{ N/cm}^2, 1.5 \text{ N/cm}^2$) added to both input images sets. (SD – Standard deviation, Tx – Translation along x axis, Ty – Translation along y axis)

Table 3: Comparison among the results obtained using the cross-correlation (CC) and phase correlation (PC), Min(XOR) and Min(MSE) (Pataky et al., 2008c), and Geometric and Hybrid registration methods (Oliveira et al., 2009b). (SD – Standard deviation)

Table 4: Comparison among the results obtained using the cross-correlation (CC) and phase correlation (PC) for inter-subjects registration.

FIGURES

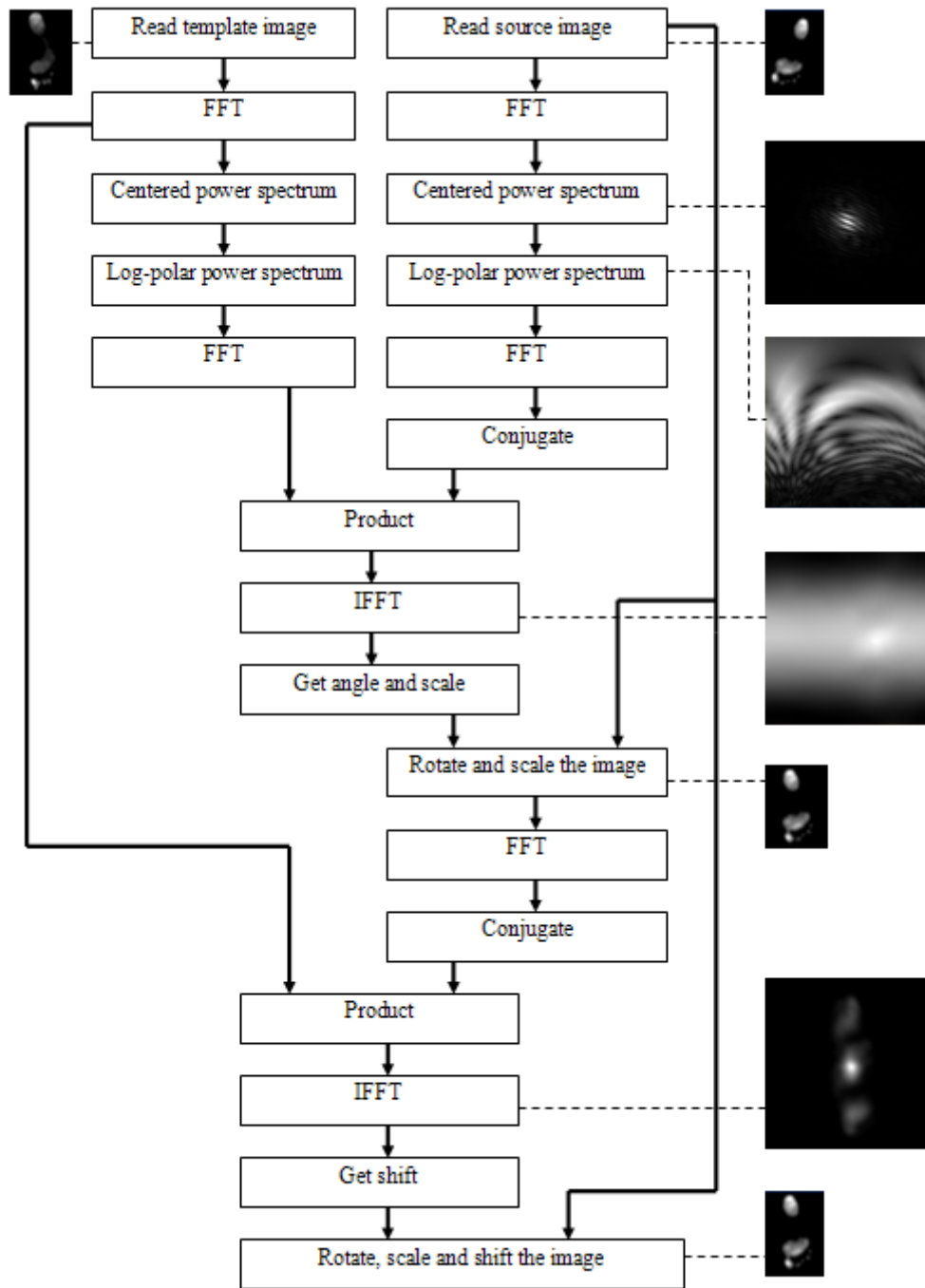


Figure 1

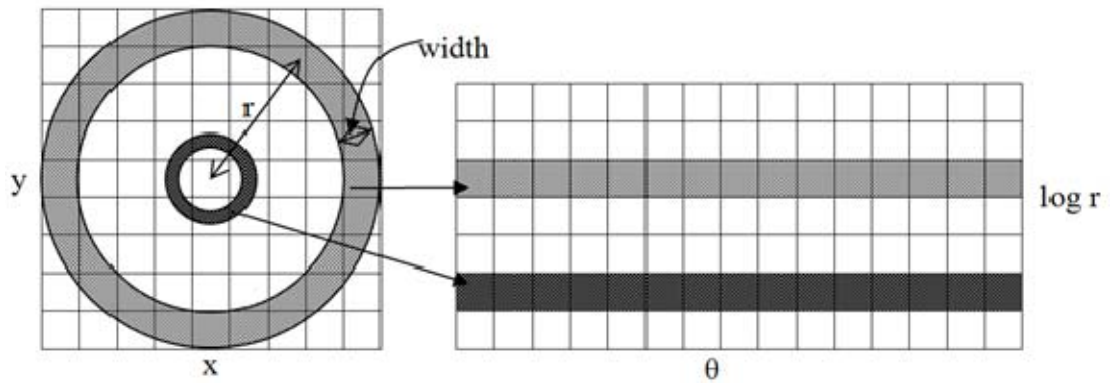


Figure 2

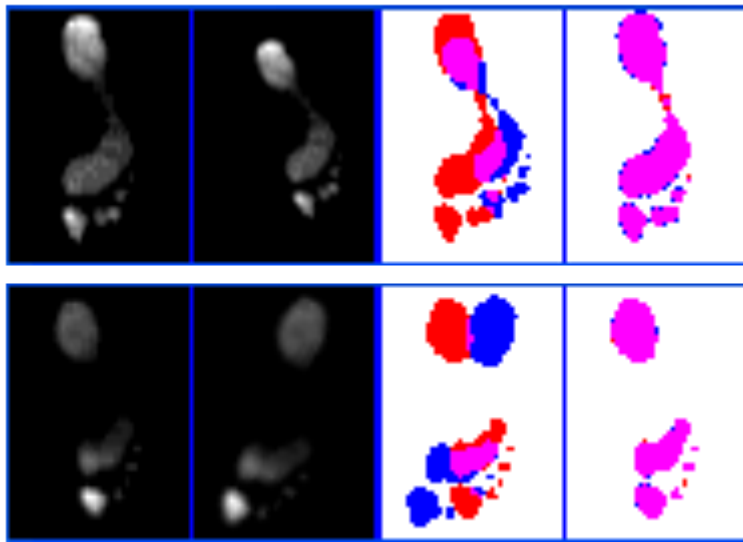


Figure 3

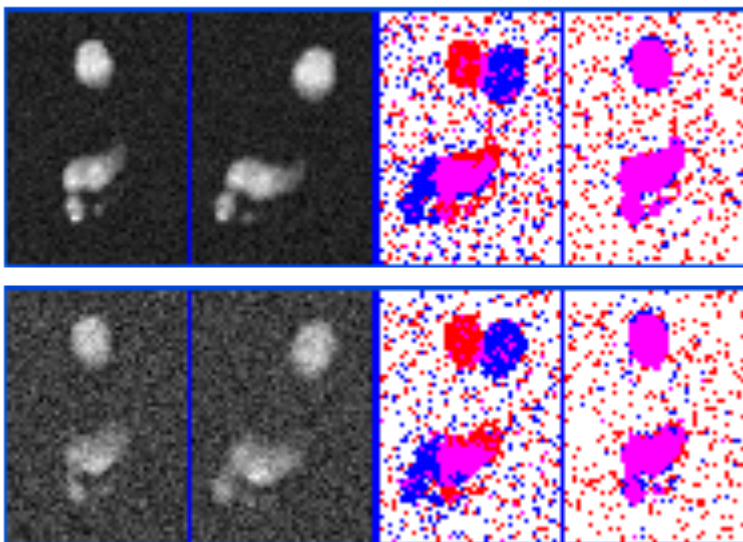


Figure 4

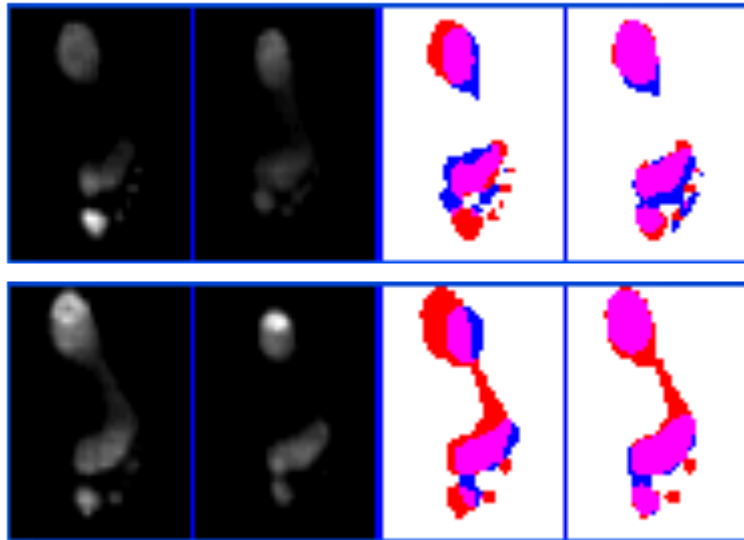


Figure 5

TABLES

Table 1

METHOD AND PARAMETERS	Angle		Scale		Tx		Ty		Time
	[°]	SD		SD	[pixel]	SD	[pixel]	SD	[ms]
Control values	-26.50		1.10		0.00		-2.50		
Method CC; logbase 1.033; angle resolution 360/256	-26.51	0.050	1.10	0.002	0.00	0.011	-2.50	0.020	41
Method CC; logbase 1.033; angle resolution 360/512	-26.50	0.049	1.10	0.001	0.00	0.011	-2.50	0.020	58
Method CC; logbase 1.12; angle resolution 360/256	-26.61	0.086	1.10	0.003	-0.01	0.027	-2.51	0.027	32
Method CC; logbase 1.12; angle resolution 360/512	-26.60	0.085	1.10	0.003	-0.01	0.028	-2.51	0.028	40
Method PC; logbase 1.033; angle resolution 360/256	-26.53	0.027	1.10	0.001	0.00	0.005	-2.49	0.014	51
Method PC; logbase 1.033; angle resolution 360/512	-26.50	0.025	1.10	0.001	0.00	0.004	-2.49	0.014	72
Method PC; logbase 1.12; angle resolution 360/256	-26.49	0.070	1.11	0.002	0.01	0.018	-2.51	0.041	39
Method PC; logbase 1.12; angle resolution 360/512	-26.47	0.087	1.11	0.004	0.02	0.023	-2.51	0.048	48
Control values	15.00		0.80		5.50		1.30		
Method CC; logbase 1.033; angle resolution 360/256	15.04	0.068	0.80	0.001	5.50	0.012	1.31	0.021	41
Method CC; logbase 1.033; angle resolution 360/512	15.02	0.066	0.80	0.001	5.50	0.012	1.31	0.021	58
Method CC; logbase 1.12; angle resolution 360/256	15.04	0.089	0.81	0.002	5.52	0.016	1.31	0.052	32
Method CC; logbase 1.12; angle resolution 360/512	15.03	0.086	0.81	0.002	5.52	0.017	1.31	0.054	40
Method PC; logbase 1.033; angle resolution 360/256	15.04	0.063	0.80	0.001	5.48	0.010	1.33	0.012	51
Method PC; logbase 1.033; angle resolution 360/512	14.99	0.072	0.80	0.001	5.48	0.009	1.33	0.012	72
Method PC; logbase 1.12; angle resolution 360/256	15.00	0.067	0.80	0.002	5.48	0.014	1.33	0.018	39
Method PC; logbase 1.12; angle resolution 360/512	14.93	0.074	0.80	0.002	5.47	0.012	1.32	0.016	48

Table 2

METHOD AND PARAMETERS	Angle		Scale		Tx		Ty	
	[°]	SD		SD	[pixel]	SD	[pixel]	SD
Control values	-26.50		1.10		0.00		-2.50	
Method: CC; logbase: 1.033; angle resolution: 360/256; noise: ($\bar{x} = 0; \sigma = 0.5$)	-26.50	0.097	1.10	0.002	0.00	0.020	-2.50	0.024
Method: CC; logbase: 1.033; angle resolution: 360/256; noise: ($\bar{x} = 0; \sigma = 1.5$)	-26.53	0.247	1.10	0.008	-0.01	0.057	-2.50	0.049
Method PC; logbase: 1.033; angle resolution: 360/256; noise: ($\bar{x} = 0; \sigma = 0.5$)	-26.53	0.066	1.10	0.001	0.00	0.016	-2.49	0.026
Method PC; logbase 1.033; angle resolution 360/256; noise ($\bar{x} = 0; \sigma = 1.5$)	-26.59	0.434	1.10	0.008	-0.02	0.092	-2.51	0.075

Table 3

METHOD AND PARAMETERS	MSE		XOR		Time
	[N/cm ²] ²	SD	%	SD	[ms]
Method CC; polar; angle resolution 360/256	4.06	2.114	12.31	1.732	33
Method CC; polar; angle resolution 360/512	4.06	2.115	12.32	1.747	41
Method PC; polar; angle resolution 360/256	4.17	2.191	12.25	1.689	39
Method PC; polar; angle resolution 360/512	4.30	2.330	12.36	1.747	50
REFERENCE RESULTS					
Min(MSE)	3.98	2.087	12.52	1.777	9010
Min(XOR)	5.45	3.289	11.60	1.725	9000
Geometric registration (using a threshold level of 10 ⁻³ N/cm ²)	5.80	3.070	11.69	2.630	25
Hybrid registration (using a threshold level of 10 ⁻³ N/cm ²)	4.52	2.320	11.09	2.520	53

Table 4

METHOD AND PARAMETERS	Average MSE [N/cm ²] ²	Average XOR [%]
Method CC; logbase 1.033; angle resolution 360/256	19.41	18.33
Method PC; logbase 1.033; angle resolution 360/256	19.43	18.57